Article

Nanostructured Fe,Co-Codoped MoO$_3$ Thin Films

Olfa Kamoun [1,*], **Amel Mami** [2], **Mohamed Aymen Amara** [1], **Ruxandra Vidu** [3,4] **and Mosbah Amlouk** [1]

1   Department of Physics, University of Tunis El Manar, 2092 Tunis, Tunisia; mohamedaymen08@gmail.com (M.A.A.); mosbah.amlouk@gmail.com (M.A.)
2   UR Photothermy, Photothermal Laboratory, Preparatory Institute for Engineering Studies of Nabeul (IPEIN), 8000 Merazka, Nabeul, Tunisia; mamiamel@gmail.com
3   Department of Electrical Engineering and Computer Science, University of California, Davis, CA 95616, USA; rvidu@ucdavis.edu
4   Faculty of Materials Sciences, University Politehnica of Bucharest, UPB-ECOMET, 011061 Bucharest, Romania
*   Correspondence: o.kamoun@yahoo.fr; Tel.: +216-4412-5082

check for updates

Abstract: Molybdenum oxide (MoO$_3$) and Fe,Co-codoped MoO$_3$ thin films obtained by spray pyrolysis have been in-depth investigated to understand the effect of Co and Fe codoping on MoO$_3$ thin films. The effect of Fe and Co on the structural, morphological and optical properties of MoO$_3$ thin films have been studied using X-ray diffraction (XRD), scanning electron microscopy (SEM), transmission electron microscopy (TEM) and energy-dispersive X-ray analysis (EDAX), optical and photoluminescence (PL) spectroscopy, and electropyroelectric methods. The XRD patterns demonstrated the formation of orthorhombic α-MoO$_3$ by spray pyrolysis. SEM characterization has shown an increase in roughness of MoO$_3$ thin films by Fe and Co doping. Optical reflectance and transmittance measurements have shown an increase in optical band gap with the increase in Fe and Co contents. Thermal conductivity and thermal diffusivity of Fe,Co-doped MoO$_3$ were 24.10–25.86 Wm^{-1}K^{-1} and 3.80×10^{-6}–5.15×10^{-6} m^{2}s^{-1}, respectively. MoO$_3$ thin films have shown PL emission. Doping MoO$_3$ with Fe and Co increases emission in the visible range due to an increase number of chemisorbed oxygen atoms. The photodegradation of an aqueous solution of methylene blue (MB) depended on the content of the codoping elements (Fe,Co). The results showed that a degradation efficiency of 90% was observed after 60 min for MoO$_3$: Fe 2%-Co 1%, while the degradation efficiency was about 35% for the undoped MoO$_3$ thin film.

Keywords: spray pyrolysis; thin films; MoO$_3$; X-ray diffraction; morphology; optical properties; transmission electron microscopy (TEM); thermal; photocatalysis

1. Introduction

Recently, nanosize molybdenum oxide has showed interesting applications. The investigation of α-MoO$_3$ nanorods obtained by hydrothermal process has shown that nanorods of about 10 μm in length and 200–300 nm in diameter can be obtained. These nanorods exhibited a significant response against triethylamine vapor with a concentration of 0.1 ppm at 300 °C [1]. Investigation of MoO$_3$ catalyst in the conversion of furfuryl alcohol (FA) and its selectivity towards dimers (C$_9$-C$_{10}$) and trimers (C$_{14}$-C$_{15}$) has shown that the FA conversion increased with the reaction time, but the selectivity decreases at longer reaction times [2]. Investigations of MoO$_{3-x}$ nanodots for medical applications have shown that the nanosized molybdenum oxide may act as a potential therapeutic material for the treatment of amyloid induced neurotoxicity [3].

The α-MoO$_3$ film obtained by spray pyrolytic deposition was recently investigated for its use in dye-sensitized solar cell (DSSC) [4]. Although MoO$_3$ films have been extensively investigated for their catalytic properties for the chemical industry and environmental remediation, only a few papers have dealt with the investigation of molybdenum oxide as counter electrode in DSSC. In fact, more attention has been paid to the study of the photocatalytic activity of the MoO$_3$ in a powder form [5–7]. In contrast, a few researches have been published describing photocatalytic performance of the molybdenum oxides thin films [8,9]. In addition, MoO$_3$ nanoparticles have been synthesized using a hydrothermal method and it was shown that the methylene blue removal is promoted by adsorption instead of photocatalytic mechanisms [6].

Over the past decade, photocatalysis technologies is the most promising for environmental purification and conversion of solar energy and ultra-violet (UV) [10–13]. Multifunctional properties such as a combination of optical, semiconducting and catalytic of metal oxides (ZnO [14] and MoO$_3$) thin films have been recently investigated. Photocatalytic properties of thin films have not been much studied until recently. M. Ponce-Mosso et al. [9] prepared amorphous MoO$_3$ thin films by radio frequency (RF) reactive magnetron sputtering, using a Mo target. The optimum photocatalytic activity was found for MoO$_3$ films deposited at different sputtering power and working pressure [9]. Molybdenum oxides are exciting materials with various applications such as optoelectronics, catalysis, sensors, superconductors, biosystems, and electrochromic systems. These oxides are obtained in several stoichiometries, among which is the MoO$_3$ stoichiometric compound with relatively wide bandgap energy (E_g = 3 eV [15–17]. MoO$_3$ may crystalize in various crystal structures such as orthorhombic, monoclinic and hexagonal, depending on how they share the MoO$_6$ octahedra, i.e., sides or corners). There are two basic polytypes of MoO$_3$: one is the orthorhombic MoO$_3$ (type R), which is a phase thermodynamically stable, and another one is a metastable monoclinic MoO$_3$ (α-type) with a ReO$_3$ type structure. The orthorhombic MoO$_3$ phase [18] is well known as a compound layered in two-dimensional planes.

Recently, molybdenum oxides have synthesized in various nano-forms such as nanorods, nanobelts, nanopores, and ultra-thin films. MoO$_3$ ultrathin films are used in smart windows and electrochemical systems. A complete overview of the structure of undoped and doped thin films based on MoO$_3$ are reported elsewhere [18–20]. In our group, MoO$_3$ thin films doped with Co and Ni [21] and Eu [20] obtained by spray pyrolysis have been throughout investigated. In this work, in order to enhance photocatalytic activity of pure MoO$_3$ thin films, we codoped MoO$_3$ thin films with iron and cobalt. In our knowledge, there are no studies reported in the literature on MoO$_3$ thin films codoped with iron and cobalt. This work presents photocatalytic behavior and physical investigations of MoO$_3$ thin films codoped with iron and cobalt obtained by spray pyrolysis. Specific emphases are put on the thermal as well as the photosensitivity [19,22–30] of such codoped films against Methyl blue dye (MB). Photocatalysis application seems to be sensitive to an appropriate codoping ratio. Our goal to use thin films is making MoO$_3$ with a rough surface that consequently increases the specific surface and can be used for photocatalysis micromachines.

2. Experimental Method

2.1. Fe-Co Codoped MoO$_3$ Thin Films Deposition

Thin films deposition was performed by spray pyrolysis at 460 °C on a glass substrate using the deposition conditions detailed by Boukhachem et al. [31]. The spraying solution consisted of 0.01 M aqueous solution of ammonium molybdate tetrahydrate [(NH$_4$)6Mo$_7$O$_{24}$4H$_2$O], and the source of iron and cobalt was iron (II) sulfate hexahydrate (FeSO$_4$, 6H$_2$O) and cobalt (II) chloride hexahydrate (CoCl$_2$, 6H$_2$O), respectively. The molar ratios (Fe/Mo) and (Co/Mo) were 0, 1 and 2%. The gas carrier was blown with nitrogen through a nozzle 0.5 mm in diameter at a pressure of 0.35 bar. The gas carrier was nitrogen, which was blown through a 0.5 mm-diameter nozzle at a pressure of 0.35 bar. The flow rate of the precursor mixture was 6.67 × 10^{-5} l/s during deposition. Following the deposition, the films were allowed to cool.

2.2. Techniques Used for the Fe-Co Codoped MoO$_3$ Thin Film Characterization

The crystallographic structure of the films was studied using a Philips PW 1729 X-ray diffractometer with Cu-Ka monochromatic radiation (λ = 0.15405 nm). A Perkin-Elmer spectrophotometer was used to study optical reflectance $R(\lambda)$ and transmittance $T(\lambda)$ within the wavelength range from 200 to 2000 nm. Scanning electron microscopy (SEM) with EDAX was used to investigate the morphology of the thin films. To determine thermal parameters of such thin films, we have used ElectroPyroElectric (EPE) technique. The measurements were performed using an excitation source in the form of modulated electrical current to generate a photothermal signal. Thermal parameters of the pyroelectric cell were reported in [31].

The photocatalytic decomposition of methylene blue (MB) was measured using two UV lamps in parallel with a total power of 16 W. The thin film sample with an area of 1 cm × 3 cm was placed in 25 mL volume of aqueous solution containing 3 mg/L MB. To establish an adsorption–desorption equilibrium, the solution was magnetically stirred in the dark for at least 30 min prior to the experiment. UV-vis spectrometer was used to quantitatively evaluate the decomposition of MB after UV illumination.

3. Structural Investigation

3.1. X-ray Diffraction Analyses

Figure 1 shows the XRD spectra of (Fe, Co) doped MoO$_3$ thin films for different doping concentrations. The peaks corresponding to the (020), (040), (131), and (261) planes agree with the orthorhombic α-MoO$_3$ structure (JCPDS card#: 76-1003), having a = 3.96 Å, b = 13.86 Å, c = 3.7 Å, and preferential orientations in the (020) and (040) directions [32,33]. The intensity of the main peak (020) increases with Fe and Co contents up to (Fe 2%, Co 1%) which indicates that the crystallinity of the MoO$_3$ thin films increases by doping. The improvement of the crystallinity with the Fe-Co codoping can be explained as follows: the Fe-Co codopants are placed in the substitutional sites which have the effect on improving the structure with an optimum for Fe 1%-Co 2%, beyond codoping Fe 1%-Co 2% it can be said that Fe-Co codopant elements have the effect of reducing the crystallinity.
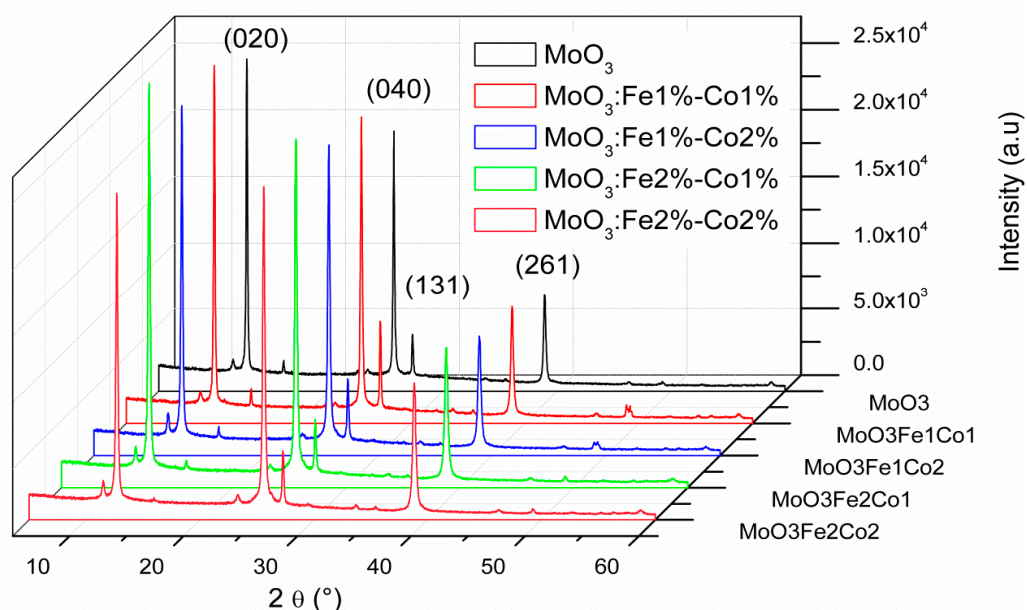
Figure 1. X-ray diffraction patterns of (Co,Fe)-doped MoO$_3$ thin films.

Additional information on the Fe-Co doping effect on the MoO_3 thin films structure was obtained by further analysis of the XRD scans. The interplanar distance d_{hkl} of MoO_3: Fe-Co thin films was calculated using the Bragg equation as follows:

$$2d_{hkl}\sin\theta = n\lambda \tag{1}$$

where n is a positive integer, λ is the wavelength of the incident wave.

The values calculated for the interplanar distance d_{hkl} for MoO_3: Fe-Co thin films are presented in Table 1. Analyzing the results obtained for MoO_3 thin films with different Fe-Co content, we observe that Fe-Co doping does not affect the d_{hkl} values. Therefore, we can assume that Fe and Co ion are substitutional dopants and do not occupy interstitial sites.

Table 1. Interplanar distance $d_{(hkl)}$ of the MoO_3: Fe-Co thin film with different codopant composition.

(hkl)	$2\theta_{hkl}$	$d_{(hkl)}$ (Å)				
		MoO_3	Fe 1% Co1%	Fe 1% Co 2%	Fe 2% Co 1%	Fe 2% Co 2%
(020)	12.73	6.95	6.94	6.94	6.94	6.94
(040)	25.58	3.48	3.47	3.47	3.47	3.47
(131)	27.29	3.26	3.26	3.26	3.26	3.26
(261)	38.88	2.31	2.31	2.31	2.31	2.31

Further, we calculated the lattice parameters a, b and c from the d_{hkl} values presented in Table 1 using the following relation [34]:

$$\frac{1}{d_{hkl}^2} = \frac{h^2}{a^2} + \frac{k^2}{b^2} + \frac{l^2}{c^2} \tag{2}$$

and the texture coefficient $TC(hkl)$, which gives the preferred orientation of the film, with the following relation [20,35,36]:

$$TC(hkl) = \frac{I(hkl)/I_0(hkl)}{N^{-1}\sum_n I(hkl)/I_0(hkl)} \tag{3}$$

where $I(hkl)$ and $I_0(hkl)$ are the measured and the standard intensity of the plane (hkl), respectively, and N is the reflection number.

Table 2 shows the $TC(hkl)$ values calculated for the MoO_3: Fe-Co thin films, where the highest values are for TC(020) and TC(040). These results indicate that the thin films are formed of crystallites parallel to the (0k0) planes.

Table 2. The texture coefficient $TC(hkl)$ calculated for the Fe-Co doped MoO_3 thin films.

(hkl)	MoO_3	TC			
		MoO_3: Fe 1% Co 1%	MoO_3: Fe 1% Co 2%	MoO_3: Fe 2% Co 1%	MoO_3: Fe 2% Co 2%
(020)	1.78	1.63	1.64	1.68	1.51
(040)	1.40	1.38	1.46	1.46	1.55
(131)	0.30	0.46	0.36	0.28	0.32
(261)	0.52	0.53	0.54	0.58	0.62

The best crystallinity is obtained for MoO_3: Fe 2%-Co 1% with preferentially orientation along (020) direction. The effect of Fe-Co dopants on the MoO_3 crystal lattice can be further analyzed by studying the crystallite size (D), the stress ξ and dislocation density δ_{dis} [35,37–40] with doping, according to the following equations:

$$D = \frac{k\lambda}{\beta_{1/2}\cos\theta} \tag{4}$$

$$\zeta = \frac{\beta cos\theta}{4} \tag{5}$$

$$\delta_{dis} = \frac{1}{D^2} \tag{6}$$

where k is the Scherrer constant (k = 0.90), $\beta_{1/2}$ is the half width of the peak (corrected value). Table 3 presents the values obtained D, ζ and δ_{dis} along (020) calculated using Equations (4)–(6).

Table 3. Caption of the stress (ζ), crystallite size (D) and dislocation density (δ_{dis}) of MoO_3: Fe-Co.

%Fe:%Co	ζ (10^{-4})	D (nm)	δ_{dis} (10^{13} lines/m^2)
0	44	82.7	15
1:1	48	77.4	17
1:2	50	71.1	20
2:1	55	65.1	24
2:2	46	69.2	21

These results show that both ζ and δ_{dis} values increase with Fe-Co codoping, while the crystallite size D shows a decrease. The codoping does not affect the lattice parameters but influences the D, ζ and δ_{dis} values. The lowest D value at 65.1 nm is obtained for MoO_3: Fe 2% Co 1%, then specific surface has increased. This result recommends the material for photocatalytic application. The highest values of the stress ζ at 55×10^{-4} and dislocation density δ_{dis} at 24×10^{13} lines/m^2 are obtained for the same material, i.e., MoO_3: Fe 2% Co 1%; the high values for ζ and δ_{dis} may be responsible for the reduced crystallite size. We can explain the highest values of ζ and δ_{dis} and the lowest value of D obtained for MoO_3: Fe 2% Co 1%, by the fact that the substitution of molybdenum cation by iron and cobalt cations is saturated at this codoping ratio and any additional Fe and Co cations take interstitial sites.

3.2. SEM-EDAX Characterization

The elemental analysis of the doped MoO_3 thin film was performed using EDAX spectra under SEM. The presence of peaks corresponding to Mo, Fe, Co and oxygen confirms the formation of MoO_3 codoped with both Fe and Co elements, Figure 2a,b. Figure 2b shows the EDX spectra of the MoO_3 obtained for the selected SEM area in Figure 2a. The characteristic energy lines for oxygen and molybdenum are located at the energies presented in Table 4. The peaks corresponding to O Kα and Mo Lα1 lines are the most intense. The composition of the film was calculated by computer software taking into account the energy lines of O K and Mo L lines for MoO_3, which corresponds to the ionized electronic shells [37].

Table 4. Characteristic energy lines for oxygen and molybdenum.

Element	O Kα	Mo Ll	Mo Lα1	Mo Lβ1	Mo Kα2	Mo Kα1	Mo Kβ1
Energy, keV	0.523	2.015	2.293	2.394	17.376	17.481	19.609

The SEM elemental mapping of MoO_3: Fe 2%-Co 1% film is shown in Figure 3 for Mo, O, Co, Fe and a map of all of them superimposed elements. The film morphology is characterized by nanoparticles uniform distributed over the surface. The energy dispersive spectroscopy (EDS) and the elemental mapping of the doped MoO_3 film demonstrate the homogeneous distribution of Mo and O elements (Figure 3a,b). Furthermore, the image presented in Figure 3e as a superimposition of the elemental mapping of all elements shows a uniform dispersion of MoO_3 nanoparticles.
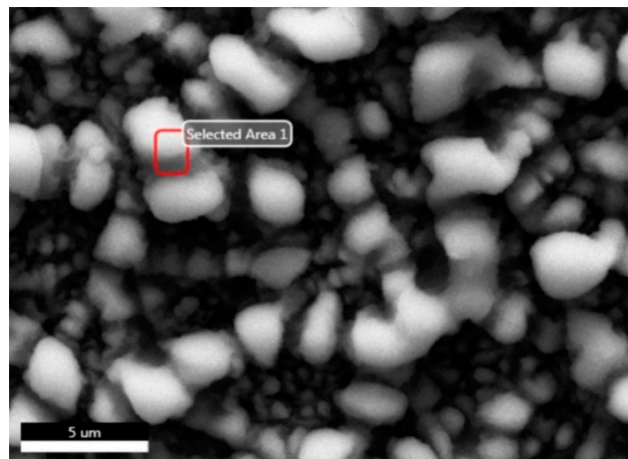
(**a**)
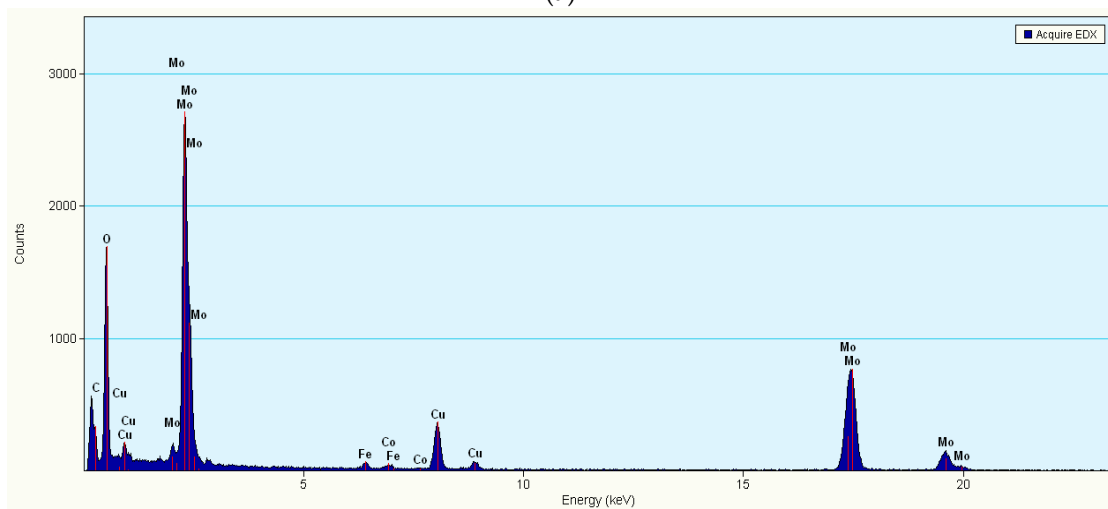
(**b**)

Figure 2. (**a**) Select area for energy-dispersive X-ray analysis (EDAX), (**b**) EDAX spectra of the MoO_3 thin film codoped Fe 2% Co 1% showing the presence of the characteristic elements.
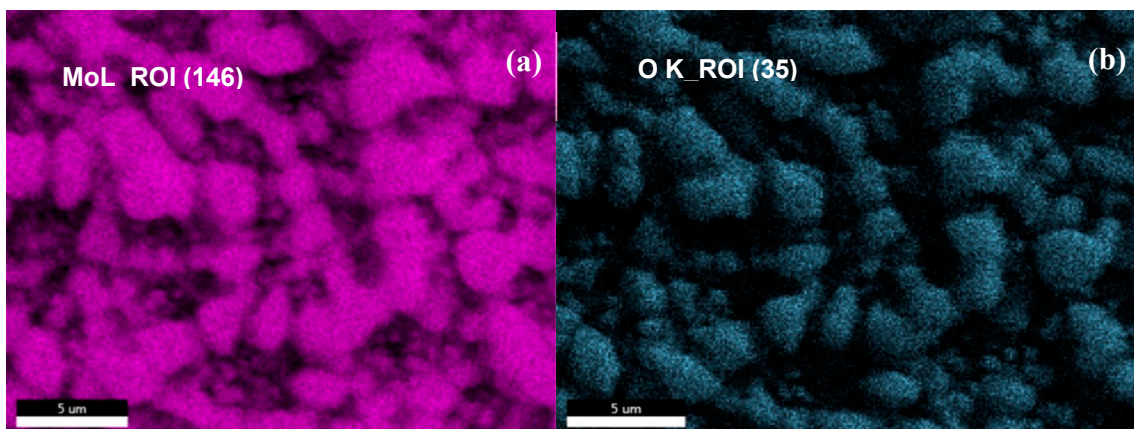
Figure 3. *Cont.*
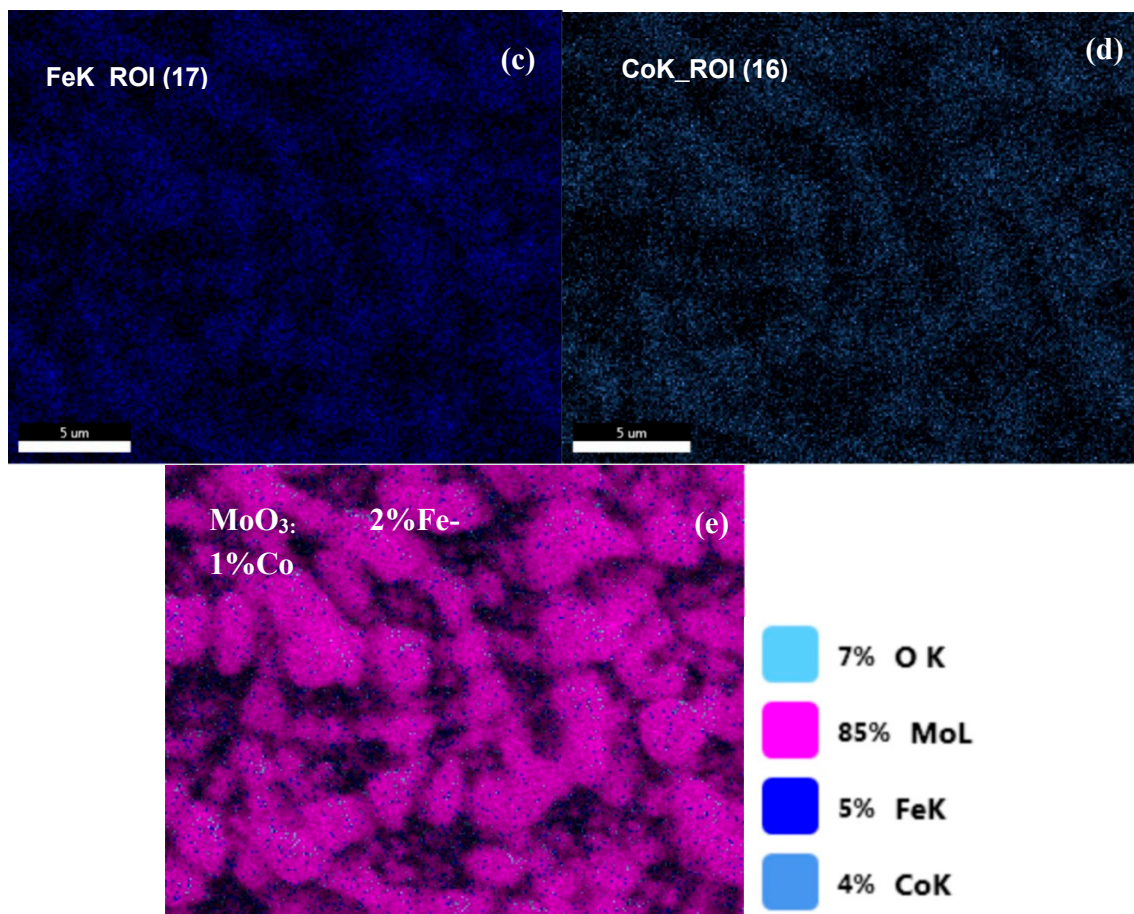
Figure 3. Scanning electron microscopy (SEM) elemental mapping of the MoO_3 surface; (**a**) pink color shows molybdenum atoms; (**b**) light blue color shows oxygen atoms; (**c**) navy blue color represents Fe present on the surface, (**d**) grey color shows the Co atoms and (**e**) MoO_3 surface mapping showing the distribution of all the elements on the surface.

3.3. SEM and TEM Observations

The SEM, TEM, high-resolution transmission electron microscopy (HRTEM), and selected area (electron) diffraction (SAED) images of MoO_3: Fe 2%-Co 1% are shown in Figures 4 and 5. Figure 4 shows a typical SEM images of α-MoO_3 film obtained by spray pyrolysis. Similar morphology of α-MoO_3 nanoplates has been observed for molybdenum oxide thin films obtained by this method [20,21]. TEM image presented in Figure 4c shows that most of α-MoO_3 plates present a four-sided plate-like shape with a length of 20–50 nm. Also, the plates seem to be stacked one over the other, the overlap being clearly seen in the SEM images.

The SAED pattern presented in Figure 5a has been indexed to α-MoO_3. Figure 5b shows the HRTEM image of the α-MoO_3, which was taken at the edge of the plate. The HRTEM image clearly indicates that the α-MoO_3 nanoplate is locally a single-crystal. The distance between the two-dimensional lattice stripes is about 0.3 nm, which is similar to that reported by Li et al. [39]. The diffraction pattern obtained from HRTEM and SAED images are similar, but the distance between the α-MoO_3 stripes differs from the 0.3 nm. The plate-like morphology of the α-MoO_3 phase is characterized by a large side-to-thickness ratios with the large surface parallel to the substrate. This morphology could cause certain defects in the structure, which could explain the distance difference between stripes when the HRTEM and SAED measurements are compared. Taking into consideration the plate morphology together with the XRD observation on preferred growth of (0k0)

planes, we can conclude that the plate-like MoO_3 crystal have the shortest side direction along the b-axis, which means that the direction of the nanoplate thickness is along the b-axis.
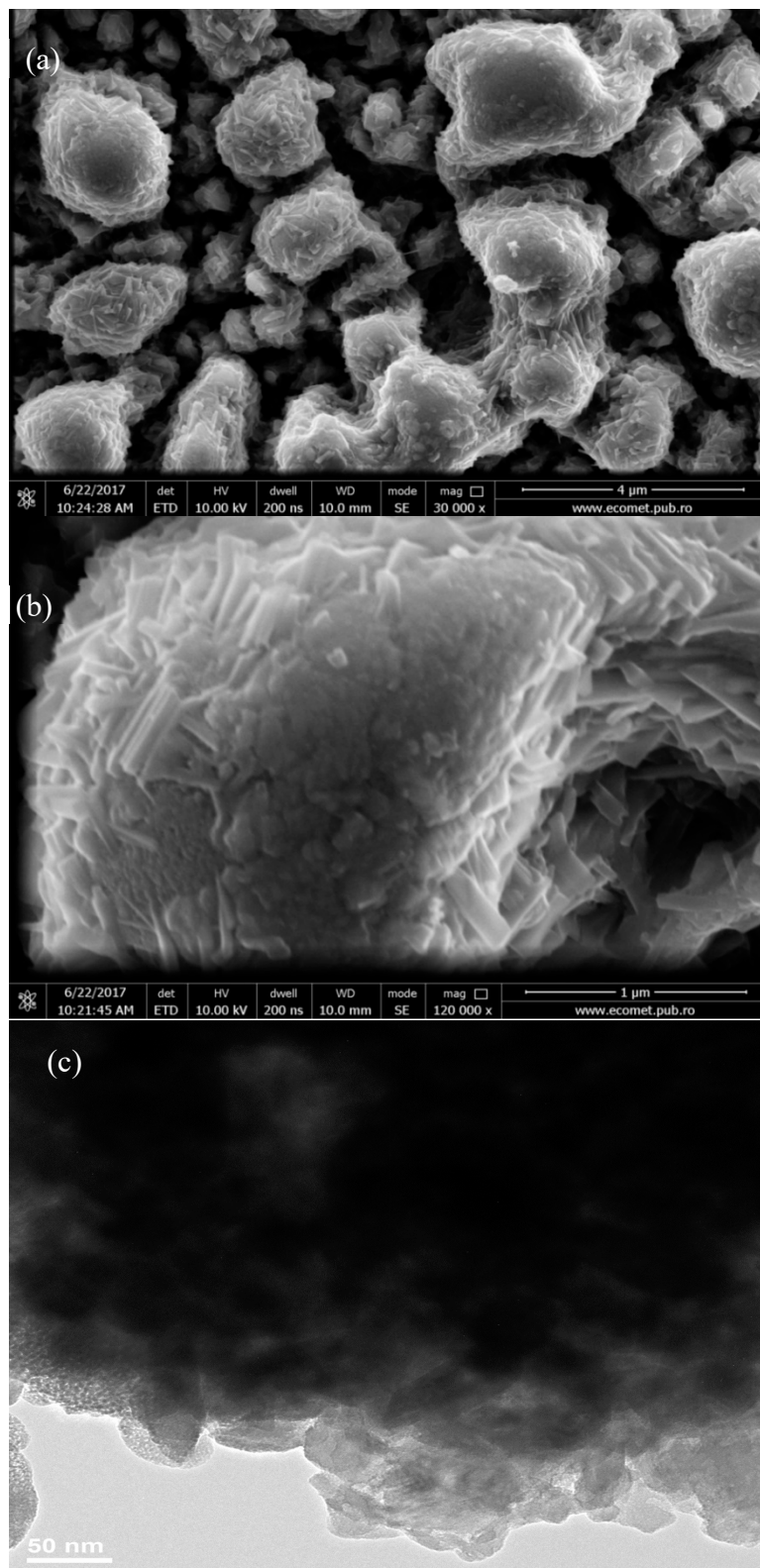
Figure 4. SEM images at 30,000× (**a**) and 120,000× (**b**) magnifications and TEM images (**c**) of the codoped MoO_3: Fe 2%-Co 1% thin films.
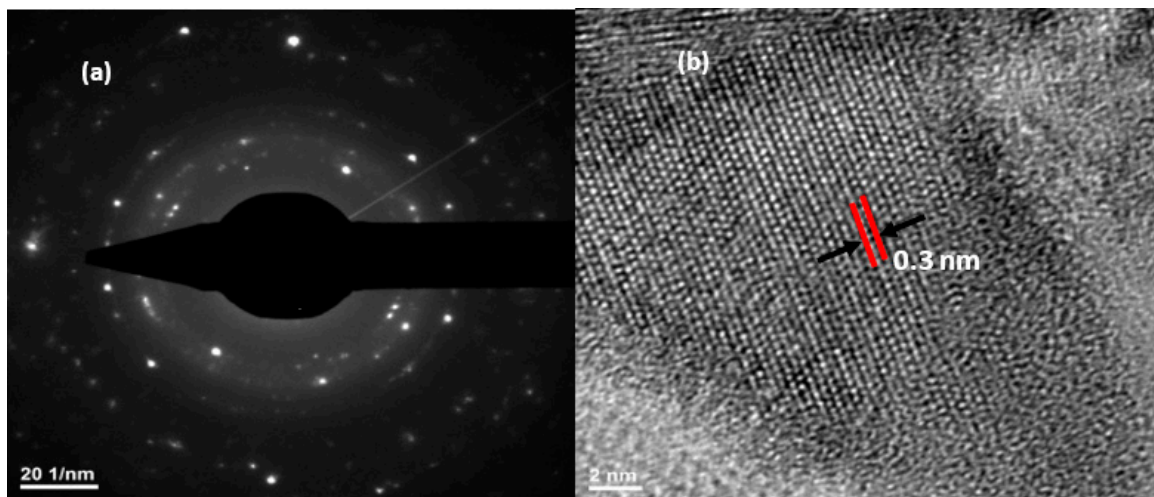
Figure 5. SAED pattern (**a**) and HRTEM image (**b**) of MoO_3: Fe 2%-Co 1%.

4. Optical Investigations

Optical investigation of the thin films was performed by measuring the transmission and reflectance. The optical transmission spectra are presented in Figure 6. In the visible range, the average transmittance of the thin films was between 40 and 75%, while the reflectance was between 7 and 37%. We observed that $T(\lambda)$ and $R(\lambda)$ spectra varies with Fe-Co content and the highest transmission in the visible range is obtained for MoO_3: Fe 2%-Co 1%. Since the transitions of electrons from the valence to the conduction band corresponds to the absorption edge, the effect of doping concentration on the optical band gap of the films can be calculated. The absorption coefficient can be expressed according to the following equation [21,41]:

$$\alpha = \frac{1}{d} Ln \frac{(1-R)^2}{T} \tag{7}$$

For a direct band gap semiconductor, the following relationship exists between band gap and absorption coefficient [42]:

$$\alpha h\nu = B\left(h\nu - E_g\right)^p \tag{8}$$

where B is a constant, E_g is the optical band gap, $h\nu$ is the incident photon energy, and p is a number which is equal to $1/2$ for direct transition. From the $(\alpha h\nu)^2$ versus $h\nu$ plots, the optical band gap E_g can be determined where the tangent to the curve intersect the *x*-axis (Figure 7). The calculated values of E_g of undoped and Fe-Co doped MoO_3 are summarized in Table 5. We observed that the E_g value increase by Fe-Co doping and the highest band gap was obtained for MoO_3: Fe 2%-Co 2%. Additionally, at energies lower than the optical gap, the optical absorption due to crystalline defects appears. Unlike crystalline structures where the adsorption edge is dictated by the difference in the valence and conduction levels, a particular optical absorption edge profile was observed by Mott et al. [43] in the ion-doped binary semiconductor compounds. The high optical transmission observed for MoO_3: Fe 2%-Co 1% means that the light penetrates better in the thin film, which can increase the total photogenerated electron-hole pairs and subsequently improves the catalyst activity.

For MoO_3 thin film, the absorption coefficient profile increases exponentially with the photon energy near the energy gap [20]. Accordingly, the band gap becomes narrow which is due to the "blurring" effect in valence and conduction bands, and the appearance of the so-called Urbach tailing [20]. Because of these interactions, the absorption coefficient is expressed by the empirical Urbach law [21,42] as follows:

$$\alpha = \alpha_0 exp\left(\frac{h\nu}{E_U}\right) \tag{9}$$

where α_0 is a constant and E_U is the Urbach energy. The E_U values presented in Table 5 show a decrease with the amount of the Fe-Co doping. This can be explained by the improvement observed in the crystallinity by Fe-Co doping as it was shown in the XRD analysis described above. The decrease of E_U by increasing Fe-Co content may be explained by a high density of states in the forbidden band, which may increase the band gap.
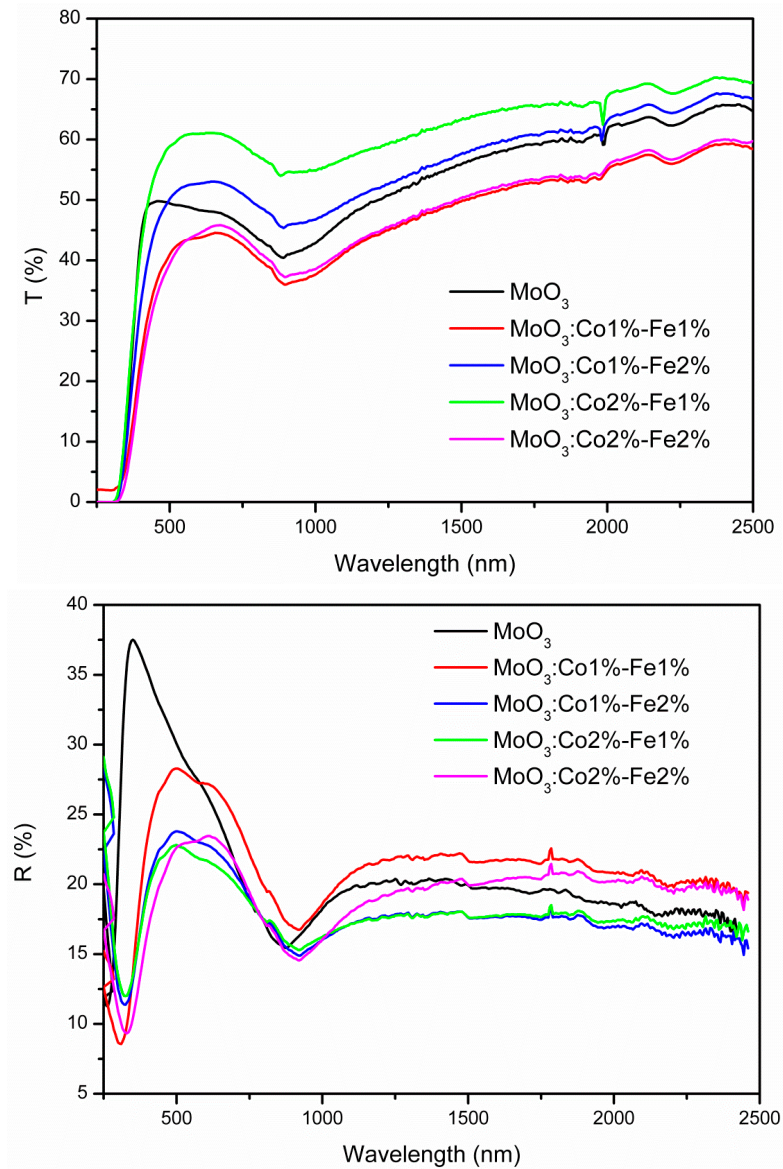
Figure 6. Transmission (T%) and reflection (R%) spectra of MoO_3: Fe-Co thin films.

Table 5. Optical band gap energy, E_g, and Urbach energy, E_U, for different content of iron and cobalt in the spray solution.

%Fe:%Co	E_g (eV)	E_U (meV)
MoO_3	3.75	370
1:1	3.80	218
1:2	3.85	245
2:1	3.88	200
2:2	3.95	150
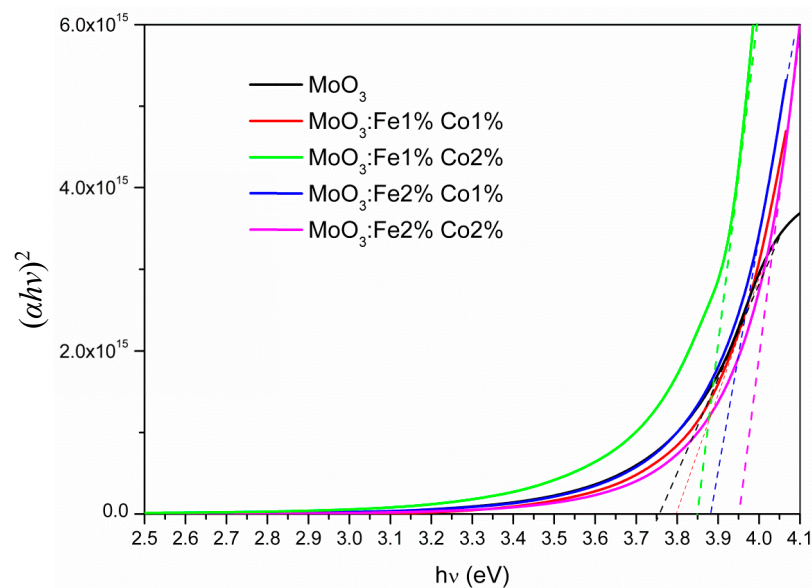
Figure 7. The $(\alpha h\nu)^2$ plot vs. $h\nu$ for MoO$_3$: Fe-Co thin films.

5. Electropyroelectric (EPE) Investigation

A literature search on the electropyroelectric behavior of the metal-oxide binary systems has provided a little information despite the use of MoO$_3$ in dye-sensitized solar cell. Because of certain possible uses of MoO$_3$ in photosensitivity applications such as thermoelectric and photocatalysis, we have investigated the thermal behavior of these thin films. The following thermal parameters have been investigated: specific heat, *C*, thermal conductivity *K*, thermal diffusivity *D* and effusivity, *e*. The relationship between these parameters are as follows:

$$C = \frac{k}{D} \tag{10}$$

$$e = (Ck)^{1/2} \tag{11}$$

The thermal conductivity and diffusivity of the thin films were measured using the ElectroPyroElectric (EPE) technique in the front detection configuration. The EPE cell used in our experiments consists of five adjacent layers as shown in reference [34]. The theoretical model of the EPE normalized voltage is a complex function that depends on the detector and frequency [44]. Figure 8 show the experimental results on normalized EPE amplitude and phase, obtained for the Co and Fe doped MoO$_3$ thin films.

Figure 9 depicts the best fit of the experimental data for the MoO$_3$ film as a function of the modulation frequency. Then, the thermal effusivity *e* and the volume heat capacity *C* can be obtained from Equations (10) and (11). The data obtained from fitting the experimental data with the theoretical values are listed in Table 6. The errors have had a rectangular distribution and were calculated statistically. The thermal conductivity for the Fe-Co codoped MoO$_3$ thin films shows an increased trend with the increase in Fe-Co codoping concentration (Table 6). The thermal diffusivity of MoO$_3$ is slightly lower than for Fe-Co codoped MoO$_3$. Consequently, the rate of the heat transfer of MoO$_3$ doped with 2% Fe and 1% Co is high. Thus, despite showing promise, MoO$_3$ film cannot surpass the thermal performance of the doped films. In addition, we observed that MoO$_3$ doped with 2% Fe and 1% Co was the best material for thermal applications, thanks to its high thermal behavior. Unfortunately, there is not much information on the thermal properties of molybdenum trioxide thin films. Thermal conductivity of molybdenum trioxide thin film sample that ranges from 24.1 to 25.86 $\mathrm{Wm^{-1}K^{-1}}$ is in good agreement with other high band gap, thermally conductive semiconductors, such as Si$_3$N$_4$ (~27 W/mK) and BN (~20 W/mK), which are unstable in an oxidizing atmosphere

and expensive to produce [45,46]. In fact, the molybdenum oxides exhibited both good Seebeck coefficient of 845 µV/K and electrical conductivity of 0.9×10^5 S/m at 80 °C [18]. Furthermore, the MoO_3 pure has an impressive thermal diffusivity of 3.8×10^{-6} m^2s with good thermal conductivity of 24.1 W/mK. Because of their thermal and electrical properties, the molybdenum oxides could be used as high-temperature thermoelectric material.
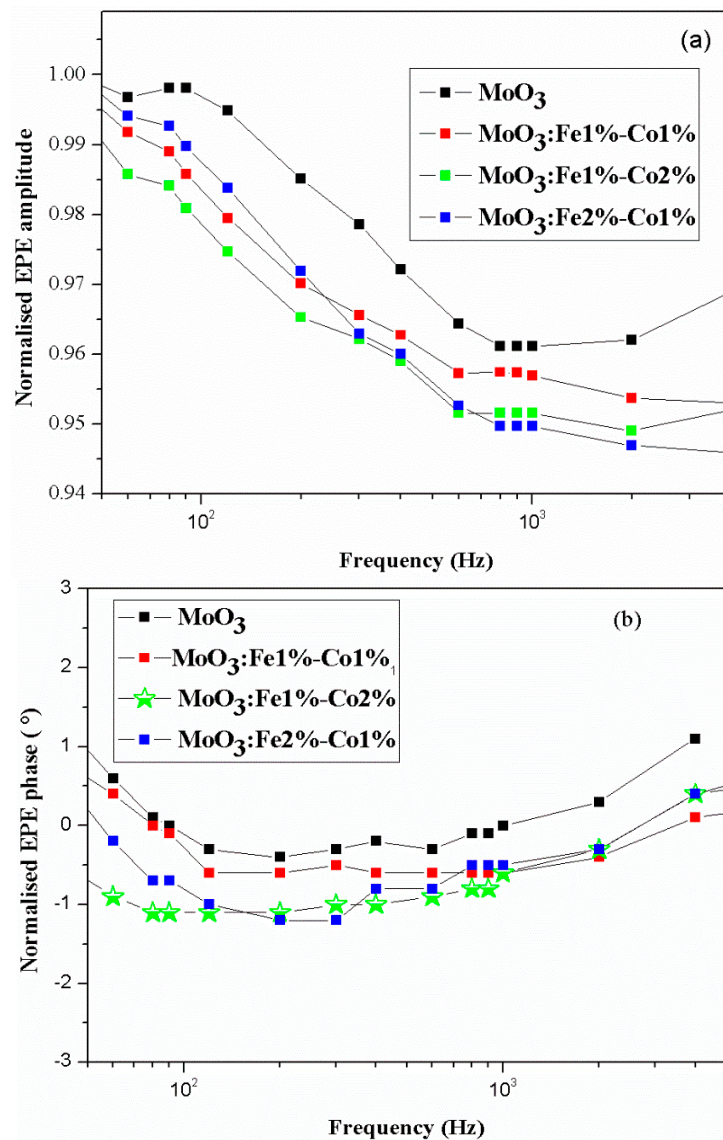
Figure 8. Experimental normalized amplitude (**a**) and phase (**b**) of the electropyroelectric signal for MoO_3 for different Fe and Co doping amount. EPE: ElectroPyroElectric.

Table 6. Thermal parameters of Fe-Co doped MoO_3.

%Fe:%Co	Thermal Conductivity K, (W/mK)	Thermal Diffusivity D, (10^{-6} m/s)	Heat Capacity C, (10^6 J/Km)	Thermal Effusivity e (10^3 J/(Km^{2}s$^{1/2}$))
0	24.10 ± 0.02	3.80 ± 0.05	6.34	12.36
1:1	25.50 ± 0.03	4.10 ± 0.04	6.21	12.59
1:2	25.62 ± 0.03	4.65 ± 0.05	5.50	11.88
2:1	25.86 ± 0.04	5.15 ± 0.05	5.02	11.39
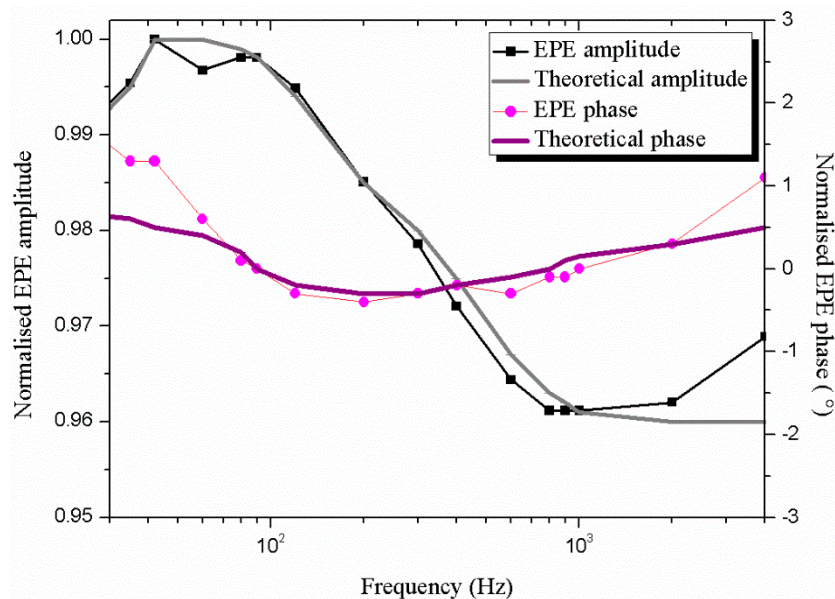
Figure 9. Experimental (dots) and theoretical (line) normalized amplitude and phase of the electropyroelectric signal according to the frequency modulation for MoO_3 sample.

6. Photoluminescence

MoO_3 thin films exhibit PL emission. Figure 10 presents the photoluminescence of doped MoO_3 along with the multi-peak Gaussian fitting of the undoped MoO_3 PL spectrum. The peaks labeled Pi, I = 1, 2, 3, . . . , 7 are located at the following wavelengths: 393, 420, 451, 486, 510, 532, and 587 nm, respectively. Molybdenum oxide exhibits luminescence peaks due to the radiative decay of self-trapped excitons. The traps are associated with certain intrinsic defects such as oxygen vacancies, or even more complex clusters of oxygen vacancies, which affects the molybdenum ion valence related to the charge transfer from O vacancies to Mo [47,48]. The peaks Pi, I = 1, 2, . . . , 7 presented in Figure 10b on the Gaussian convoluted PL spectra of MoO_3 corresponding to the free excitons recombination are in agreement with the published literature data [48,49]. The transitions positioned at 451, 486, 510, and 532 nm could be associated with the Mo^{6+} d–d band transition [49–51].

The broad features of the PL peaks may be due to the band bending effect at the film surface. Since MoO_3 is an oxygen sensor with high affinity towards oxygen at room temperature, chemisorptions of oxygen occur when MoO_3 films is exposed to air. The oxygen adsorption will capture the electrons from the surface, resulting in band bending [52]. When excited, the photogenerated electrons near the surface move across the depletion region in the opposite directions, which reduces their chances of recombination [52]. Simultaneously, the holes move to the surface where they interact with the adsorbed oxygen ions. The physisorbed oxygen is less stable than the adsorbed oxygen and therefore is likely to be desorbed from the surface, thus reducing the band gap and emitting in the visible range. which results in visible emission. Doping MoO_3 with Fe and Co increases emission in the visible range due to an increase number of chemisorbed oxygen atoms. The PL spectrum of the film presented in Figure 10 shows an interesting aspect in that the intensity of the peak in the visible range is stronger than the UV near-band-edge peak. When the film is Fe-Co codoped, the intensity of the emission peak is stronger compared to the undoped MoO_3 film. The largest PL peaks where observed for MoO_3: Fe 2%-Co 1%this can be due to an increase of oxygen vacancy by codoping. This observation leads to the conclusion that the UV and visible luminescence centers are not related.
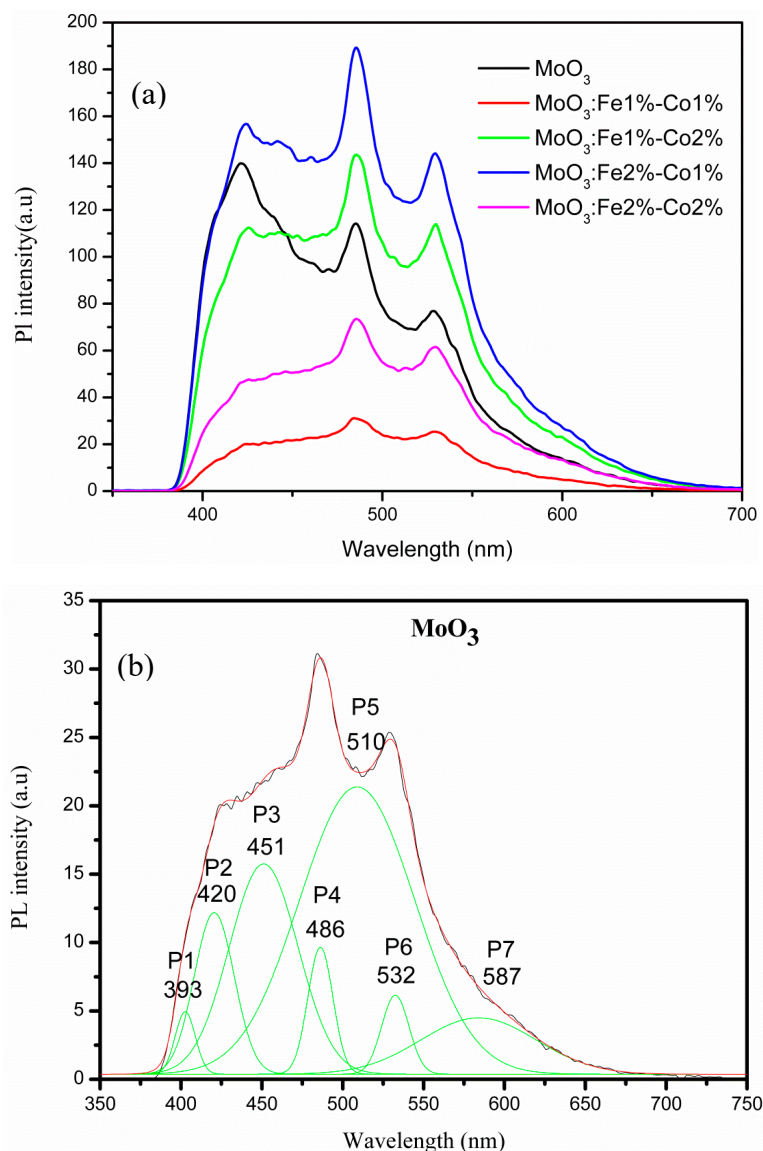
Figure 10. Photoluminescence of MoO₃: Fe-Co (**a**) and (**b**) Gaussien convolution of PL spectra undoped MoO₃.

7. Photocatalytic Performance

In this work, the photocatalytic decomposition of methylene blue was used to test and compare the photocatalytic performance of the undoped and Fe-Co codoped MoO_3. The absorption spectra of MB solution UV irradiated for 1 h is presented in Figure 11. There are two absorption peaks that correspond to methylene blue (MB), i.e., at 609 and 660 nm [53]. The peak located at 660 nm is so high for MoO_3: Fe 2%-Co 2%, the intensity of this pic varies with Fe-Co content, but it becomes so low for MoO_3: Fe 2%-Co 1% sample which indicates the best decomposition of MB dye solution [54]. Figure 12 presents the time-dependence of the absorption spectra (Figure 12a), the degradation efficiency (Figure 12b), and the degradation kinetics of MB solution in the presence MoO_3: Fe 2%-Co 1% thin film (Figure 12c). After 1 h irradiation, about 90% of the MB amount was degraded by MoO_3: Fe 2%-Co 1% (Figure 12a), compared to 35% degradation in the presence of the undoped MoO_3 film.

The degradation efficiency of MoO_3 (Fe,Co) thin films of MB dye is given in Figure 12b. The degradation efficiency of MoO_3 (Fe,Co) was calculated using the following expression [55],

$$Degradation efficiency (\%) = \frac{C_0 - C}{C_0} \qquad (12)$$

where, C_0 is the initial concentration of dye solution, and C is the concentration of dye solution after irradiation in the selected time interval [55].

The rate at which a pollutant is removed from the aqueous solution can be predicted by the reaction kinetics of MB dye, which can be was evaluated using Equation (13) [56]:

$$Ln\frac{C}{C_0} = -kt \tag{13}$$

Figure 12c shows the plot of $Ln(C/C_0)$ versus the irradiation time. It can be observed that the $Ln(C/C_0)$ varies linearly with time, which indicates that the photodegradation of MB dye follows the first-order kinetics [56].
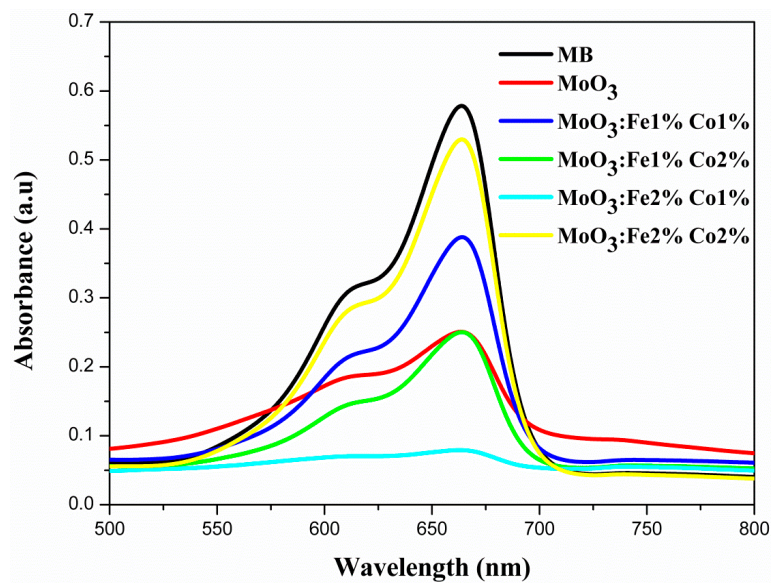
Figure 11. Absorption spectra of methylene blue (MB) solution under UV light after 1 h.
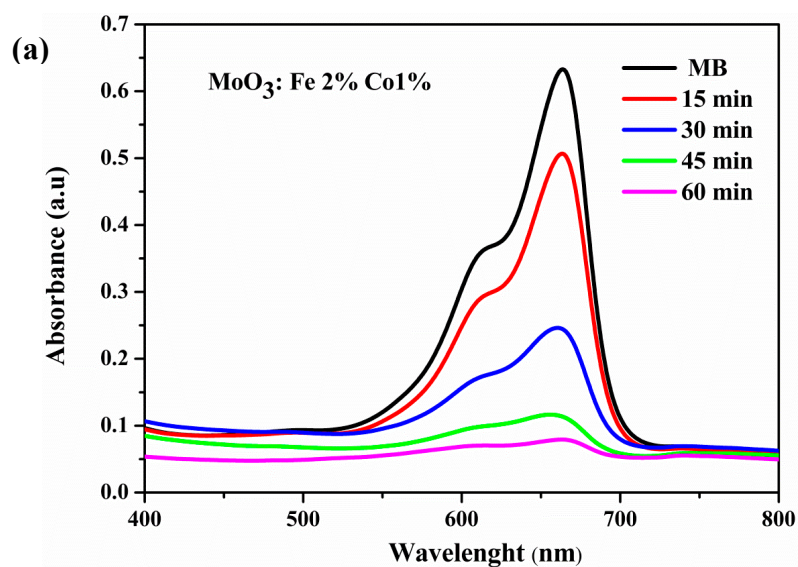
Figure 12. *Cont.*
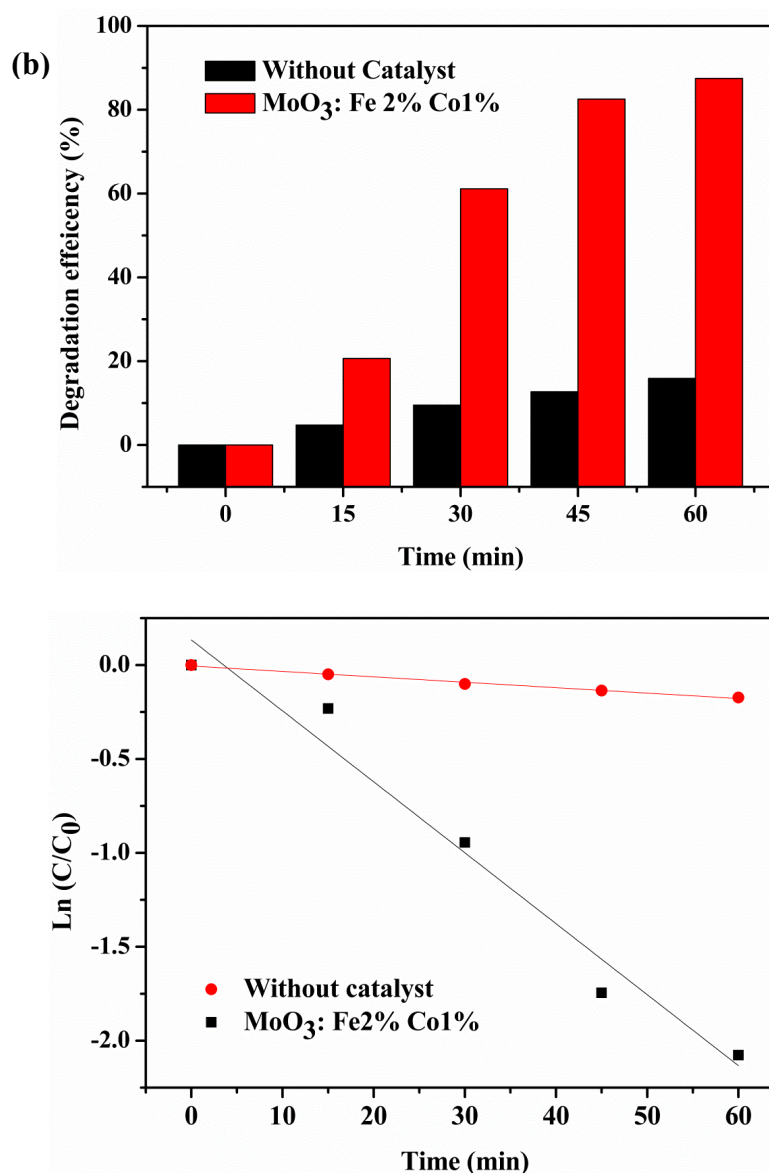
Figure 12. Time-dependent absorption spectra (**a**) of MB dye solution in the presence MoO_3: Fe 2%-Co 1% (**b**) degradation efficiency and (**c**) degradation kinetics of MB dye.

8. Conclusions

This comprehensive study on MoO_3 and Fe-Co codoped MoO_3 thin films obtained by spray pyrolysis presents results having a key information for industrial applications. The detailed nanostructural and morphological studies showed the formation of α-MoO_3 structure with an interesting laminar crystallization within the layers, which forms nanoplates as observed by SEM, TEM, HRTEM, and SAED. While the Fe-Co codoping does not affect significantly the crystallite size, it increases the density of dislocation and stresses the film.

These crystallographic effects induced by doping are found in the optical studies. Transmission and reflection measurements have shown that the absorption edges of the film vary with doping concentration. The band gap energy value of the Fe-Co codoped MoO_3 increases with Fe-Co codoping.

Electropyrolytic measurements performed on the thin films have demonstrated a metallic character that is not so sensitive to the Fe:Co ratio in the doped films. It is found that the thermal conductivity of MoO_3 has a remarkable value of 24.1 $Wm^{-1}K^{-1}$ with a thermal diffusivity value of 3.8×10^{-6} m^2s^{-1}. Moreover, it is found that MoO_3 codoped with 2% Fe-1% Co has the highest

thermal conductivity. Due to their high thermal behavior, these results recommend the Fe-Co codoped molybdenum oxides as high-temperature thermoelectric materials.

MoO_3 and Fe-Co Codoped MoO_3 thin films present a rough surface with randomly oriented islet-like morphology, which is in particular important for the observed photocatalytic activity of MoO_3: Fe 2%-Co 1%. The photodegradation measurements of the films against MB dye has shown a remarkable increase in the photosensitivity of MoO_3: Fe 2%-Co 1%. We believe that the photosensitivity of the MoO_3: Fe 2%-Co 1% thin film increase is due to a small excess in iron content, which could be explained by the following processes: (i) a small amount of iron could oxidize to produce Fe_2O_3 as a minority phase distributed randomly in the film, which improves the photocatalytic activity of the film; (ii) an excess of free carriers located near the conduction band could be formed in the MoO_3: Fe 2%-Co 1% thin film, which enhances the photocatalysis behavior of the film; (iii) both phenomena could occur and the effect have cumulative enhancement action on the photocatalytic properties of the film.

This comprehensive study on undoped and Fe-Co codoped MoO_3 thin films presents very interesting results especially those related to multifunctional properties such as optical, thermal and photocatalytic properties of this particular thin film system, which outweigh the increase in these proprieties, as would be expected from doping. Further studies are in progress to elucidate the remarkable effect of codoping on certain properties of MoO_3 that are relevant to specific applications. Combined with low cost spray pyrolysis process, this technology has a considerable potential in reducing the cost of integrating metal oxide semiconductor thin films into devices.

References

1.　He, S.; Li, W.; Feng, L.; Yang, W. Rational interaction between the aimed gas and oxide surfaces enabling high-performance sensor: The case of acidic α-MoO_3 nanorods for selective detection of triethylamine. *J. Alloys Compd.* **2019**, *783*, 574–582. [CrossRef]

2.　Chan, X.; Akter, N.; Yang, P.; Ooi, C.; James, A.; Boscoboinik, J.A.; Parise, J.B.; Kim, T. Fundamental study of furfuryl alcohol dehydration reaction over molybdenum oxide catalyst. *Mol. Catal.* **2019**, *466*, 19–25. [CrossRef]

3.　Han, Q.; Wang, X.; Liu, X.; Zhang, Y.; Cai, S.; Qi, C.; Wang, C.; Yang, R. MoO_{3-x} nanodots with dual enzyme mimic activities as multifunctional modulators for amyloid assembly and neurotoxicity. *J. Colloid Interface Sci.* **2019**, *539*, 575–584. [CrossRef] [PubMed]

4.　Tamboli, P.S.; Jagtap, C.V.; Kadam, V.S.; Ingle, R.V.; Vhatkar, R.S.; Mahajan, S.S.; Pathan, H.M. Spray pyrolytic deposition of α-MoO_3 film and its use in dye-sensitized solar cell. *Appl. Phys. A* **2018**. [CrossRef]

5.　Manivel, A.; Lee, G.-J.; Chen, C.-Y.; Chen, J.-H.; Ma, S.-H.; Horng, T.-L.; Wu, J.J. Synthesis of MoO_3 nanoparticles for azo dye degradation by catalytic ozonation. *Mater. Res. Bull.* **2015**, *62*, 184–191. [CrossRef]

6.　Santos-Beltrán, M.; Paraguay-Delgado, F.; García, R.; Antúnez-Flores, W.; Ornelas-Gutiérrez, C.; Santos-Beltrán, A. Fast methylene blue removal by MoO_3 nanoparticles. *J. Mater. Sci. Mater. Electron.* **2016**, *28*, 2935–2948. [CrossRef]

7.　　Unnarkat, A.P.; Sridhar, T.; Wang, H.; Mahajani, S.M.; Suresh, A.K. Study of cobalt molybdenum oxide supported on mesoporous silica for liquid phase cyclohexane oxidation. *Catal. Today* **2018**, *310*, 116–129. [CrossRef]

8.　　Dhara, A.; Hodes, G.; Sarkar, S.K. Two stage chemical bath deposition of MoO_3 nanorod films. *RSC Adv.* **2014**, *4*, 53694–53700. [CrossRef]

9.　　Ponce-Mosso, M.; Pérez-González, M.; García-Tinoco, P.E.; Crotte-Ledesma, H.; Morales-Luna, M.; Tomás, S.A. Enhanced photocatalytic activity of amorphous MoO_3 thin films deposited by rf reactive magnetron sputtering. *Catal. Today* **2018**. [CrossRef]

10.　Di, L.; Yang, H.; Xian, T.; Chen, X. Construction of Z-Scheme $g-C_3N_4/CNT/Bi_2Fe_4O_9$ Composites with Improved Simulated-Sunlight Photocatalytic Activity for the Dye Degradation. *Micromachines* **2018**, *9*, 613. [CrossRef]

11.　Fox, M.A.; Dulay, M.T. Heterogeneous photocatalysis. *Chem. Rev.* **1993**, *93*, 341–357. [CrossRef]

12.　Kudo, A. Development of photocatalyst materials for water splitting. *Int. J. Hydrogen Energy* **2006**, *31*, 197–202. [CrossRef]

13.　Zhang, Y.; Liu, J.; Chen, D.; Qin, Q.; Wu, Y.; Huang, F.; Li, W. Preparation of FeOOH/Cu with High Catalytic Activity for Degradation of Organic Dyes. *Materials* **2019**, *12*, 338. [CrossRef] [PubMed]

14.　Laurenti, M.; Cauda, V. Porous Zinc Oxide Thin Films: Synthesis Approaches and Applications. *Coatings* **2018**, *8*, 67. [CrossRef]

15.　Chen, Y.; Lu, C.; Xu, L.; Ma, Y.; Hou, W.; Zhu, J.-J. Single-crystalline orthorhombic molybdenum oxide nanobelts: Synthesis and photocatalytic properties. *CrystEngComm* **2010**, *12*, 3740–3747. [CrossRef]

16.　Qu, Q.; Zhang, W.-B.; Huang, K.; Chen, H.-M. Electronic structure, optical properties and band edges of layered MoO_3: A first-principles investigation. *Comput. Mater. Sci.* **2017**, *130*, 242–248. [CrossRef]

17.　Zheng, Z.; Chen, J.; Wang, Y.; Wang, X.; Chen, X.; Liu, P.; Xu, J.; Xie, W.; Chen, H.; Deng, S.; et al. Highly Confined and Tunable Hyperbolic Phonon Polaritons in Van Der Waals Semiconducting Transition Metal Oxides. *Adv. Mater.* **2018**, *30*, e1705318. [CrossRef]

18.　De Castro, I.A.; Datta, R.S.; Ou, J.Z.; Castellanos-Gomez, A.; Sriram, S.; Daeneke, T.; Kalantar-Zadeh, K. Molybdenum Oxides—From Fundamentals to Functionality. *Adv. Mater.* **2017**, *29*. [CrossRef]

19.　Boukhachem, A.; Mokhtari, M.; Benameur, N.; Ziouche, A.; Martínez, M.; Petkova, P.; Ghamnia, M.; Cobo, A.; Zergoug, M.; Amlouk, M. Structural optical magnetic properties of Co doped $\alpha-MoO_3$ sprayed thin films. *Sens. Actuators A Phys.* **2017**, *253*, 198–209. [CrossRef]

20.　Kamoun, O.; Boukhachem, A.; Amlouk, M.; Ammar, S. Physical study of Eu doped MoO_3 thin films. *J. Alloys Compd.* **2016**, *687*, 595–603. [CrossRef]

21.　Kamoun, O.; Boukhachem, A.; Alleg, S.; Jeyadevan, B.; Amlouk, M. Physical study of nano-structured MoO_3 films codoped with cobalt and nickel in which there is a ferro-diamagnetic transition. *J. Alloys Compd.* **2018**, *741*, 847–854. [CrossRef]

22.　Alizadeh, S.; Hassanzadeh-Tabrizi, S.A. MoO_3 fibers and belts: Molten salt synthesis, characterization and optical properties. *Ceram. Int.* **2015**, *41*, 10839–10843. [CrossRef]

23.　Chithambararaj, A.; Bose, A.C. Investigation on structural, thermal, optical and sensing properties of meta-stable hexagonal MoO(3) nanocrystals of one dimensional structure. *Beilstein J. Nanotechnol.* **2011**, *2*, 585–592. [CrossRef] [PubMed]

24.　Chithambararaj, A.; Sanjini, N.S.; Velmathi, S.; Bose, A.C. Preparation of $h-MoO_3$ and $alpha-MoO_3$ nanocrystals: Comparative study on photocatalytic degradation of methylene blue under visible light irradiation. *Phys. Chem. Chem. Phys.* **2013**, *15*, 14761–14769. [CrossRef] [PubMed]

25.　He, T.; Yao, J. Photochromism of molybdenum oxide. *J. Photochem. Photobiol. C Photochem. Rev.* **2003**, *4*, 125–143. [CrossRef]

26.　Hsu, C.-S.; Chan, C.-C.; Huang, H.-T.; Peng, C.-H.; Hsu, W.-C. Electrochromic properties of nanocrystalline MoO_3 thin films. *Thin Solid Film.* **2008**, *516*, 4839–4844. [CrossRef]

27.　Li, J.; Liu, X. Preparation and characterization of $\alpha-MoO_3$ nanobelt and its application in supercapacitor. *Mater. Lett.* **2013**, *112*, 39–42. [CrossRef]

28.　Li, T.; Zeng, W.; Zhang, Y.; Hussain, S. Nanobelt-assembled nest-like MoO_3 hierarchical structure: Hydrothermal synthesis and gas-sensing properties. *Mater. Lett.* **2015**, *160*, 476–479. [CrossRef]

29. Subba Reddy, C.V.; Qi, Y.Y.; Jin, W.; Zhu, Q.Y.; Deng, Z.R.; Chen, W.; Mho, S.-I. An electrochemical investigation on (MoO$_3$+PVP+PVA) nanobelts for lithium batteries. *J. Solid State Electrochem.* **2007**, *11*, 1239–1243. [CrossRef]

30. Subbiah, J.; Kim, D.Y.; Hartel, M.; So, F. MoO$_3$/poly(9,9-dioctylfluorene-co-N-[4-(3-methylpropyl)]-diphenylamine) double-interlayer effect on polymer solar cells. *Appl. Phys. Lett.* **2010**, *96*. [CrossRef]

31. Boukhachem, A.; Bouzidi, C.; Boughalmi, R.; Ouerteni, R.; Kahlaoui, M.; Ouni, B.; Elhouichet, H.; Amlouk, M. Physical investigations on MoO$_3$ sprayed thin film for selective sensitivity applications. *Ceram. Int.* **2014**, *40*, 13427–13435. [CrossRef]

32. Cao, B.; Wang, X.; Rino, L.; Wu, J.; He, Y.; Feng, Z.; Dong, B. Morphology and upconversion properties of rare-earth-doped MoO$_3$ jellyfish-like plate microarchitecture. *Mater. Lett.* **2018**, *213*, 4–6. [CrossRef]

33. Kolodziej, M.; Lalik, E.; Colmenares, J.C.; Lisowski, P.; Gurgul, J.; Duraczyńska, D.; Drelinkiewicz, A. Physicochemical and catalytic properties of Pd/MoO$_3$ prepared by the sonophotodeposition method. *Mater. Chem. Phys.* **2018**, *204*, 361–372. [CrossRef]

34. Martínez, H.M.; Torres, J.; López Carreño, L.D.; Rodríguez-García, M.E. Effect of the substrate temperature on the physical properties of molybdenum tri-oxide thin films obtained through the spray pyrolysis technique. *Mater. Charact.* **2013**, *75*, 184–193. [CrossRef]

35. Arifa, H.; Boukhachem, A.; Askri, B.; Boubaker, K.; Yumak, A.; Raouadi, K. Structural, optical and conductivity investigations on κ-Al$_2$O$_3$ ceramics for powder metallurgical production and sensitivity applications. *Ceram. Int.* **2016**, *42*, 2147–2157. [CrossRef]

36. Boukhachem, A.; Ouni, B.; Karyaoui, M.; Madani, A.; Chtourou, R.; Amlouk, M. Structural, opto-thermal and electrical properties of ZnO:Mo sprayed thin films. *Mater. Sci. Semicond. Process.* **2012**, *15*, 282–292. [CrossRef]

37. Angeles-Chavez, C.; Toledo-Antonio, J.A.; Cortes-Jacome, M.A. Chemical quantification of Mo-S, W-Si and Ti-V. energy dispersive X-ray spectroscopy. In *X-ray Spectroscopy*; Sharma, S.K., Ed.; IntechOpen: London, UK, 2012; pp. 119–136. [CrossRef]

38. Kamoun, O.; Boukhachem, A.; Mrabet, C.; Yumak, A.; Petkova, P.; Boubaker, K.; Amlouk, M. Effect of europium content on physical properties of In$_2$O$_3$ thin films for sensitivity and optoelectronic applications. *Bull. Mater. Sci.* **2016**, *39*, 777–788. [CrossRef]

39. Li, X.-L.; Liu, J.-F.; Li, Y.-D. Low-temperature synthesis of large-scale single-crystal molybdenum trioxide (MoO$_3$) nanobelts. *Appl. Phys. Lett.* **2002**, *81*, 4832–4834. [CrossRef]

40. Bouzidi, C.; Sdiri, N.; Boukhachem, A.; Elhouichet, H.; Férid, M. Impedance analysis of BaMo$_{1-x}$W$_x$O$_4$ ceramics. *Superlattices Microstruct.* **2015**, *82*, 559–573. [CrossRef]

41. Tauc, J. *The Optical Properties of Solids*; Academic: Waltham, MA, USA, 1966.

42. Urbach, F. The Long-Wavelength Edge of Photographic Sensitivity and of the Electronic Absorption of Solids. *Phys. Rev.* **1953**, *92*, 1324. [CrossRef]

43. Mott, N.F.; Davis, E.A. *Electronic Processes in Non-Crystalline Materials*; Clarendon Press: Oxford, UK, 1979.

44. Mami, A.; Mellouki, I.; Ben Mbarek, M.; Amlouk, M.; Yacoubi, N. Deep Thermal Investigations on Ag2S Thin Film Along with Electropyroelectric and Photothermal Deflection Techniques. *IEEE Sens. J.* **2016**. [CrossRef]

45. Borca-Tasciuc, D.-A.; Chen, G.; Prieto, A.; Martín-González, M.S.; Stacy, A.; Sands, T.; Ryan, M.; Fleurial, J. Thermal properties of electrodeposited bismuth telluride nanowires embedded in amorphous alumina. *Appl. Phys. Lett.* **2004**, *85*, 6001–6003. [CrossRef]

46. Lee, S.; Kang, S. Effect of a ZnO addition on the thermal properties of diopside-based glass ceramics for LED packages. *Contemp. Eng. Sci.* **2016**, *9*, 1425–1436. [CrossRef]

47. Minoru, I.; Kousuke, H.; Shuji, O. Optical properties and electronic structures of layered MoO$_3$ single crystals. *J. Phys. Condens. Matter* **2001**, *13*, 6853.

48. Zhao, Y.; Liu, J.; Zhou, Y.; Zhang, Z.; Xu, Y.; Naramoto, H.; Yamamoto, S. Preparation of MoO$_3$ nanostructures and their optical properties. *J. Phys. Condens. Matter* **2003**, *15*, L547–L552. [CrossRef]

49. Rabindar, K.S.; Reddy, G.B. Synthesis and characterization of α-MoO$_3$ microspheres packed with nanoflakes. *J. Phys. D Appl. Phys.* **2014**, *47*, 065305.

50. Dieterle, M.; Mestl, G. Raman spectroscopy of molybdenum oxides. *Phys. Chem. Chem. Phys.* **2002**, *4*, 822–826. [CrossRef]

51. Łabanowska, M. Paramagnetic defects in MoO$_3$—Revisited. *Phys. Chem. Chem. Phys.* **1999**, *1*, 5385–5392. [CrossRef]

52. Navas, I.; Vinodkumar, R.; Mahadevan Pillai, V.P. Self-assembly and photoluminescence of molybdenum oxide nanoparticles. *Appl. Phys. A* **2011**, *103*, 373–380. [CrossRef]

53. Song, L.X.; Xia, J.; Dang, Z.; Yang, J.; Wang, L.B.; Chen, J. Formation, structure and physical properties of a series of α-MoO$_3$ nanocrystals: From 3D to 1D and 2D. *CrystEngComm* **2012**, *14*. [CrossRef]

54. Wongkrua, P.; Thongtem, T.; Thongtem, S. Synthesis of h- andα-MoO$_3$ by Refluxing and Calcination Combination: Phase and Morphology Transformation, Photocatalysis, and Photosensitization. *J. Nanomater.* **2013**, *2013*, 79. [CrossRef]

55. Krishnaprasanth, A.; Seetha, M. Solvent free synthesis of Ta$_2$O$_5$ nanoparticles and their photocatalytic properties. *AIP Adv.* **2018**, *8*, 055017. [CrossRef]

56. Mageshwari, K.; Mali, S.S.; Sathyamoorthy, R.; Patil, P.S. Template-free synthesis of MgO nanoparticles for effective photocatalytic applications. *Powder Technol.* **2013**, *249*, 456–462. [CrossRef]